THE JOURNAL OF PHYSICAL CHEMISTRY LETTERS
A JOURNAL OF THE AMERICAN CHEMICAL SOCIETY

pubs.acs.org/JPCL

Letter

Enormous and Tunable Bulk Charge/Spin Photovoltaic Effect in Piezoelectric Binary Materials T-IV-VI and T-V-V

Chengwei Liao, Minglong Wang, and Yu-Jun Zhao*

Cite This: J. Phys. Chem. Lett. 2024, 15, 6099−6107

Read Online

ACCESS | Metrics & More | Article Recommendations | Supporting Information

ABSTRACT: Understanding the nonlinear response of light and materials is crucial for fundamental physics and next-generation electronic devices. In this work, we have investigated the second-order nonlinear bulk photovoltaic (BPV) and bulk spin photovoltaic (BSPV) effects in the piezoelectric binary materials T-IV-VI and T-V-V (IV = Ge, Sn; VI = S, Se; and V = P, As, Sb, Bi). The independent nonzero conductivity tensors of charge current are derived for these binaries through the symmetry analysis, along with the mechanism for generating pure spin current. These binaries, with their unique folded structure, exhibit significant charge and spin currents under illumination. Furthermore, we find that strain engineering can effectively modulate charge/spin currents by influencing charge density distribution and built-in electric field due to the piezoelectric effect. Our research suggests that the piezoelectric binary materials possess enormous and tunable charge/spin currents, underscoring their potential for applications in nonlinear flexible optoelectronics and spintronics.

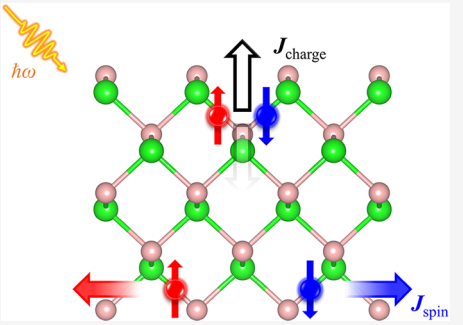

With the rapid advancement of laser technology, research on the nonlinear optical response of light and matter has gained interest in physics and engineering. The bulk photovoltaic (BPV) effect, a second-order nonlinear optical response, directly converts light into direct current (DC) within homogeneous materials.[1−5] The BPV effect can generate voltages exceeding the material's band gap, and the conversion efficiency is not limited by the Shockley−Queisser limit,[6,7] making it a promising candidate for energy harvesting and photodetection.[8−10] The bulk spin photovoltaic (BSPV) effect,[11−15] analogous to BPV effect, generates spin currents under illumination, offering advantages for data storage and quantum computing.[16−18] The BPV and BSPV effects require breaking of the spatial inversion symmetry (*P*-symmetry) in the system. Usually, ferroelectric and piezoelectric functional materials are prone to breaking the *P*-symmetry, making them popular candidates for studying second-order nonlinear optical responses.[4,15,19−22]

Recently, Lei et al. discovered tricycle-phase T-IV-VI (IV = Ge, Sn; VI = S, Se) structures similar to the α-phase group IV monochalcogenides.[23] These structures demonstrate good thermal/dynamical and excellent piezoelectric performance, such as $d_{11} \sim 452.3$ pm/V in T-SnS. Similarly, Guo et al. recently uncovered piezoelectric materials, denoted as T-V-V (V = P, As, Sb, Bi), which possess the same structural configurations and valence electrons as T-IV-VI.[24] T-V-V exhibits intrinsic persistent spin helix (PSH)[25] characteristics and a unidirectional spin configuration, T-V-V holds promise for applications in spintronic devices. T-IV-VI and T-V-V exhibit outstanding piezoelectric properties and distinctive spin characteristics. However, the nonlinear optical responses within them, as well as the coupling relationship between BPV (BSPV) and the piezoelectric effect, remain unclear. For brevity, this work will use T-XY to denote this class of T-phase piezoelectric binary materials T-IV-VI and T-V-V (IV = Ge, Sn; VI = S, Se; and V = P, As, Sb, Bi).

In this work, we have utilized first-principles calculations and nonlinear optical response theory to investigate the BPV and BSPV effects in the piezoelectric material T-XY. We analyze the physical mechanisms of charge current and spin current generation in T-XY through group theory and structure symmetry analysis. The piezoelectric material T-XY exhibits enormous photoconductivity of charge/spin currents. The maximum photoconductivity of T-XY is 1−2 orders of magnitude greater than that of typical 2D materials, owing to its unique triple-staggered layers structure. Finally, we propose that strain engineering can effectively control the magnitude of charge/spin photocurrents in T-XY.

The theoretical framework of BPV and BSPV effects are compared. The BPV effect, accounting for the charge degree of freedom of electrons, results in a generated charge current that can be divided into two parts: shift current (SC) induced by linearly polarized light (LPL) and injection current (IC) induced by circularly polarized light (CPL). Here, we primarily

Received: April 29, 2024
Revised: May 24, 2024
Accepted: May 29, 2024
Published: May 31, 2024

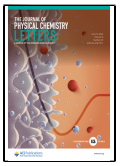

https://doi.org/10.1021/acs.jpclett.4c01257
J. Phys. Chem. Lett. 2024, 15, 6099−6107

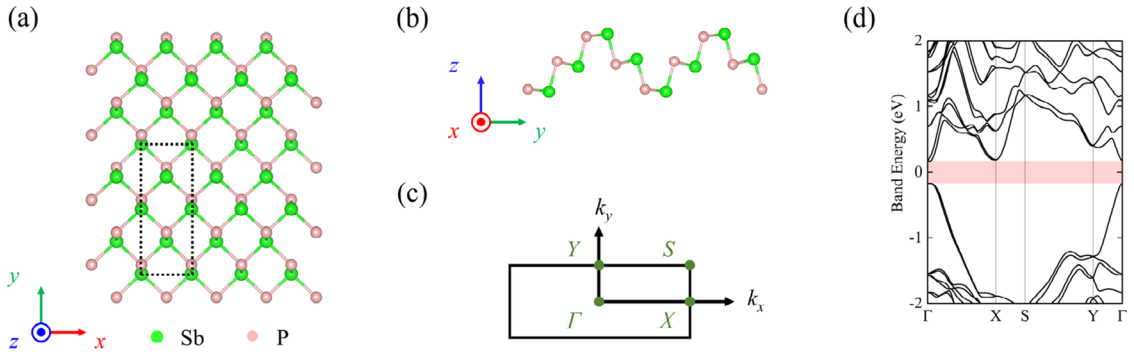

Figure 1. Atomic and electronic structures of T-SbP. (a) Top view of the atomic structure, with the black dashed rectangle representing the unit cell. (b) Side view of the atomic structure. (c) First Brillouin zone. (d) Band structure. The red shaded area indicates the band gap.

emphasize the photoconductivity, as knowing only the frequency and intensity of the incident light allows us to obtain the photocurrent. In systems with broken *P*-symmetry and preserved time-reversal symmetry (*T*-symmetry), according to the Kubo response theory,[26,27] under the independent-particle approximation, the conductivities for SC and IC can be expressed as[28−31]

$$\sigma_{bc}^{a} = -\frac{\pi e^3}{2\hbar^2}\int_{BZ}\frac{d^3\boldsymbol{k}}{(2\pi)^3}\sum_{m,n} f_{nm} R_{nm}^{a,b} r_{nm}^{b} r_{mn}^{c} \delta(\omega_{mn} - \omega) \tag{1}$$

$$\eta_{bc}^{a} = \frac{\pi e^3}{2\hbar^2}\int_{BZ}\frac{d^3\boldsymbol{k}}{(2\pi)^3}\sum_{m,n} f_{nm} \Delta_{nm}^{a} \Omega_{mn}^{bc} \delta(\omega_{mn} - \omega) \tag{2}$$

where a represents the direction of the current, b and c represent the directions of the optical electric field, and ω denotes the frequency of the light. The difference in the electron occupation between the m and n energy bands is denoted by $f_{nm} = f_n - f_m$, and the energy difference is denoted by $\hbar\omega_{mn}$. In σ_{bc}^{a}, $R_{nm}^{a,b} = \frac{\partial \phi_{nm}^{b}}{\partial k_a} - A_{nn}^{a} + A_{mm}^{a}$ is the shift vector, while $r_{nm}^{b} r_{mn}^{c} = |r_{nm}^{b}|^2$ is the transition rate (for LPL, $b = c$). Interband Berry connection $r_{nm}^{b} = |r_{nm}^{b}| e^{i\phi_{nm}^{b}} = \frac{v_{nm}^{b}}{i\omega_{nm}}$ ($n \neq m$), ϕ_{nm}^{b} is the phase factor of r_{nm}^{b}, and $v_{nm}^{b} = \langle n|\partial H/\partial k_b|m\rangle$ is the interband velocity matrix. $A_{nn}^{a} = i\langle n|\partial H/\partial k_a|n\rangle$ is the intraband Berry connection matrix. In η_{bc}^{a}, $\Delta_{nm}^{a} = v_{nn}^{a} - v_{mm}^{a}$ is the group velocity difference, and $\Omega_{mn}^{bc} = i[r_{mn}^{b}, r_{nm}^{c}] = i(r_{mn}^{b} r_{nm}^{c} - r_{mn}^{c} r_{nm}^{b})$ is the Berry curvature.

The BSPV effect is essentially a counterpart of the BPV effect, focusing on the spin degree of freedom of electrons and resulting in the generation of spin currents. For BPV, electron spin properties (up/down) are not distinguished, leading to charge current generation, whereas BSPV involves spin operators, resulting in the generation of pure spin currents. The conductivity of spin photocurrent under LPL and CPL can be expressed as[32−34]

$$\sigma_{bc}^{a,S^i} = -\tau\frac{\pi e^2}{\hbar^2}\int_{BZ}\frac{d^3\boldsymbol{k}}{(2\pi)^3}\sum_{m,n} f_{nm} \Delta j_{mn}^{a,i} g_{nm}^{bc} \delta(\omega_{mn} - \omega) \tag{3}$$

$$\eta_{bc}^{a,S^i} = i\frac{\pi e^2}{\hbar^2}\int_{BZ}\frac{d^3\boldsymbol{k}}{(2\pi)^3}\sum_{m,n,l} f_{lm}\frac{v_{lm}^{b}}{\omega_{ml}^{2}}\left(\frac{j_{mn}^{a,i} v_{nl}^{c}}{\omega_{mn}} - \frac{v_{mn}^{c} j_{nl}^{a,i}}{\omega_{nl}}\right)\delta(\omega_{ml} - \omega) \tag{4}$$

where the superscript i denotes the spin polarization direction. In the equations $j_{mn}^{a,i} = \frac{1}{2}\{v_{mn}^{a}, s_{nm}^{i}\} = \frac{1}{2}(v_{mn}^{a} s_{nm}^{i} + s_{mn}^{i} v_{nm}^{a})$ is the spin current operator. Here, $s_{nm}^{i} = \frac{\hbar}{2}\langle n|\sigma^i|m\rangle$ is the spin operator and σ^i is the Pauli matrix. $\Delta j_{mn}^{a,i} = j_{mm}^{a,i} - j_{nn}^{a,i}$ is the spin velocity difference between bands m and n. $g_{nm}^{bc} = \{r_{nm}^{b}, r_{mn}^{c}\} = r_{nm}^{b} r_{mn}^{c} + r_{nm}^{c} r_{mn}^{b}$ is the quantum metric.

Here are important notes before photoconductivity calculations. The BPV/BSPV conductivity only considers interband contributions, with the Dirac δ function $\delta(\omega_{mn} - \omega)$ representing resonant transitions of interband electrons under optical excitation. The SC is a static current, independent of the carrier lifetime τ, whereas the IC initially grows with time and reaches saturation in the static limit; thus, the effective conductivity of IC should be defined as $\tau\eta_{bc}^{a}$.[31] To ensure comparability between charge current and spin current, we introduce a factor $\hbar/2e$ in the units of spin current conductivity.[35] See the Supporting Information for more details about the first-principles calculation and nonlinear responses calculation procedures.

The atomic structure of monolayer T-SbP is illustrated in the top and side views, as depicted in Figure 1a,b, respectively. The following studies on T-XY are exemplified with T-Sb, which is in analogy to other T-XY structures. In the top view, both α-phase and T-phase exhibit the same bonding configuration. Sb(P) atoms are bonded to three adjacent P(Sb) atoms. The dashed rectangle in Figure 1a represents the unit cell, with lattice parameters of a = 3.83 Å and b = 8.96 Å, consistent with structural optimization as reported in prior studies.[23,24] The lattice parameters for other T-XY structures are provided in Supporting Information Table S1. In the side view, T-SbP consists of triple-staggered layers of Sb−P atoms, forming a chairlike shape along the y-direction. The space group of T-SbP is $Pmc2_1$ (No. 26), with a point group of C_{2v}. Monolayer T-SbP possesses four symmetric operations: (1) the identity operation E; (2) mirror symmetry operation M_x, where the mirror plane is parallel to the yz plane and perpendicular to the x-axis; (3) 2-fold rotation symmetry operation $\{C_{2x}|(1/2a, 1/2b, 0)\}$, with the rotation axis lying in the xy plane and perpendicular to the x-axis; (4) mirror symmetry operation $\{M_z|(1/2a, 1/2b, 0)\}$, where the mirror plane is parallel to the xy plane and perpendicular to the z-axis.

The first Brillouin zone and band structure of T-SbP are depicted in Figure 1c,d, respectively. In the band structure, the shaded area in red indicates the band gap region, which measures 0.332 eV. The band structure of T-XY is illustrated in

https://doi.org/10.1021/acs.jpclett.4c01257
J. Phys. Chem. Lett. 2024, 15, 6099−6107

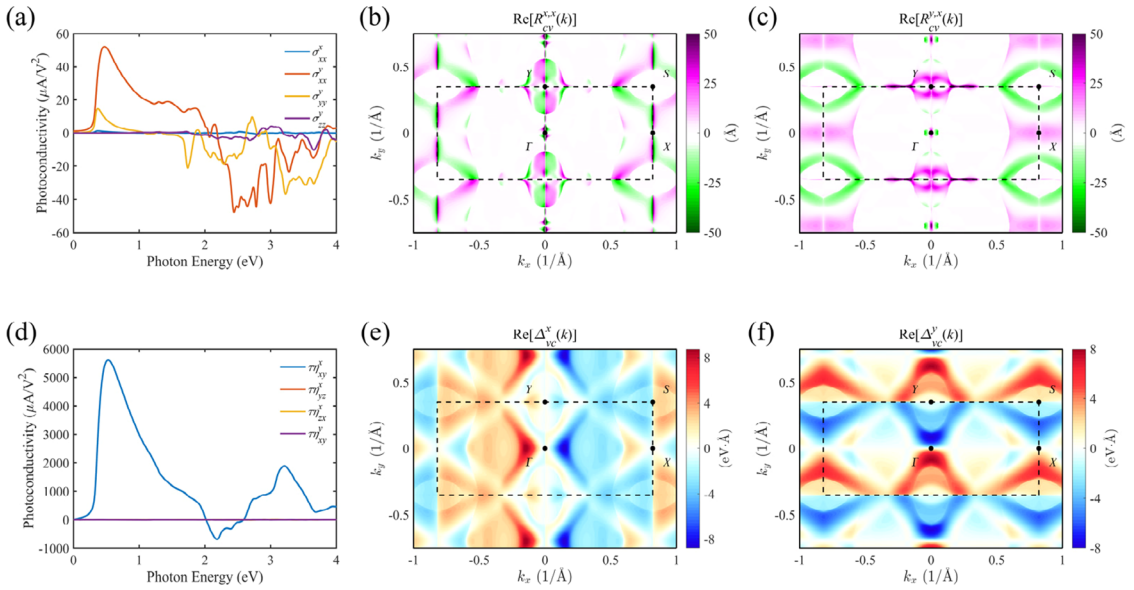

Figure 2. Charge current and the distribution of physical quantities in momentum space for T-SbP. (a) The SC photoconductivity σ^x_{xx}, σ^y_{xx}, σ^y_{yy}, and σ^y_{zz}. (b) $\boldsymbol{k}$-solved shift vector of σ^x_{xx}, between the valence band v and the conduction band c. (c) $\boldsymbol{k}$-solved shift vector of σ^y_{xx}. (d) IC photoconductivity $\tau\eta^x_{xy}$, $\tau\eta^x_{yz}$, $\tau\eta^x_{zx}$ and $\tau\eta^y_{xy}$. (e) $\boldsymbol{k}$-solved velocity difference of $\tau\eta^x_{xy}$. (f) $\boldsymbol{k}$-solved velocity difference of $\tau\eta^y_{xy}$.

Supporting Information Figure S1. Taking into account the spin−orbit coupling (SOC) interaction, the band gap range for T-XY is between 0.031 and 1.422 eV (as listed in Table S1). Furthermore, we further investigated the atomic orbital projection of T-SbP near the Fermi level, as depicted in Figure S2. The VBM is predominantly occupied by the 5s and 5p_z orbitals of Sb atoms, as well as the 3p_y and 3p_z orbitals of P atoms, while the CBM is mainly contributed by the 5p_y orbitals of Sb and the 3s and 3p_z orbitals of P. Previous theoretical calculations have revealed that the piezoelectric material T-XY exhibits excellent thermodynamic and kinetic stabilities.[23,24] Therefore, selecting appropriate substrates and synthesis methods during experimentation to fabricate this structure holds great promise.[36,37]

The point group of monolayer T-SbP is C_{2v}, lacking spatial inversion symmetry, thus permitting second-order nonlinear optical response. Under the P-symmetry, $PR_{nm}(\boldsymbol{k}) = -R_{nm}(-\boldsymbol{k})$, $Pr_{nm}\, r_{mn}(\boldsymbol{k}) = r_{nm}r_{mn}(-\boldsymbol{k})$, $P\Delta_{mn}(\boldsymbol{k}) = -\Delta_{mn}(-\boldsymbol{k})$, and $P\Omega_{mn}(\boldsymbol{k}) = \Omega_{mn}(-\boldsymbol{k})$. The P-symmetry ensures that both σ^a_{bc} and η^a_{bc} in BPV effect are odd functions at $\boldsymbol{k}$ and $-\boldsymbol{k}$, resulting in the integral of conductivity over the entire Brillouin zone to zero and thus the disappearance of current. Conversely, under the T-symmetry, $Tv_{nm}(\boldsymbol{k}) = -v^*_{nm}(-\boldsymbol{k})$, $Tr_{nm}(\boldsymbol{k}) = r^*_{nm}(-\boldsymbol{k}) = r_{mn}(-\boldsymbol{k})$, $TR_{nm}(\boldsymbol{k}) = -R^*_{nm}(-\boldsymbol{k}) = -R_{mn}(-\boldsymbol{k}) = R_{nm}(-\boldsymbol{k})$, $Tr_{nm}r_{mn}(\boldsymbol{k}) = r_{nm}r_{mn}(-\boldsymbol{k})$, $T\Delta_{mn}(\boldsymbol{k}) = -\Delta_{mn}(-\boldsymbol{k})$, and $T\Omega_{mn}(\boldsymbol{k}) = -\Omega_{mn}(-\boldsymbol{k})$; * indicates a complex conjugate, where σ^a_{bc} and η^a_{bc} are both even functions at $\boldsymbol{k}$ and $-\boldsymbol{k}$. Subsequently, we will employ group theory to analyze the C_{2v} point group and discuss the independent nonzero conductivity tensor of T-SbP.

The character table of the C_{2v} point group is provided in Table S2. It is noteworthy that the standard character table employs traditional coordinate definitions, which differ from the custom coordinates defined in this work (as shown in Figure 1a). In this work, the x-direction corresponds to the traditional y-direction (y to z, and z to x). Since the polarization intensity $\boldsymbol{P}$, current density $\boldsymbol{J}$, and electric field $\boldsymbol{E}$ are all polar vectors, they share the same irreducible representation, $\Gamma_{\boldsymbol{P}} = \Gamma_{\boldsymbol{J}} = \Gamma_{\boldsymbol{E}} = A_1 + B_1 + B_2$. The relationship between linear polarization intensity and electric field is given by $\boldsymbol{P} = \chi^{(1)}\boldsymbol{E}$, where $\chi^{(1)}$ is the linear susceptibility. The direct product of the irreducible representations of the polarization intensity and electric field is

$$\Gamma_{\boldsymbol{P}} \otimes \Gamma_{\boldsymbol{E}} = (A_1 + B_1 + B_2) \otimes (A_1 + B_1 + B_2) = 3A_1 + 2A_2 + 2B_1 + 2B_2$$

where $3A_1$ indicates that the linear susceptibility $\chi^{(1)}$ has three independent nonzero components.[38]

The current density of SC under LPL illumination is $\boldsymbol{J}^{(2)}_{\mathrm{SC}} = \sigma^{(2)}\boldsymbol{EE}$; the electric field of light with no phase difference is $\Gamma_{\boldsymbol{E}} \otimes \Gamma_{\boldsymbol{E}} = \Gamma_{\boldsymbol{P}} \otimes \Gamma_{\boldsymbol{E}}$. The direct product of electric fields can be divided into symmetric part $(3A_1 + A_2 + B_1 + B_2)^s$ and antisymmetric part $(A_2 + B_1 + B_2)^{as}$. Here, we only need to consider the symmetric part,

$$\Gamma_{J_{\mathrm{SC}}} \otimes (\Gamma_{\boldsymbol{E}} \otimes \Gamma_{\boldsymbol{E}})^s = 5A_1 + 3A_2 + 5B_1 + 5B_2$$

indicating that the SC conductivity $\sigma^{(2)}$ has five independent nonzero components. For example,

$$\Gamma_{J^y_{\mathrm{SC}}} \otimes \Gamma_{E_x} \otimes \Gamma_{E_x} = A_1 \otimes B_2 \otimes B_2 = A_1$$

$\sigma^y_{xx} \neq 0$, others $\sigma^y_{yy} \neq 0$ and $\sigma^y_{zz} \neq 0$, as shown in Table S3. Besides the LPL-xx (yy, zz), the LPL-xy representing linearly polarized light at a 45° angle with respect to the x and y coordinates, $\Gamma_{J^x_{\mathrm{SC}}} \otimes \Gamma_{E_x} \otimes \Gamma_{E_y} = A_1$, $\Gamma_{J^z_{\mathrm{SC}}} \otimes \Gamma_{E_y} \otimes \Gamma_{E_z} = A_1$, $\sigma^x_{xy} \neq 0$, and $\sigma^z_{yz} \neq 0$.

The current density of IC under CPL illumination is $\boldsymbol{J}^{(2)}_{\mathrm{IC}} = \eta^{(2)}\boldsymbol{E} \times \boldsymbol{E}^*$; there exists a phase difference i between

https://doi.org/10.1021/acs.jpclett.4c01257
J. Phys. Chem. Lett. 2024, 15, 6099−6107

electric fields E_b and E_c, $(\Gamma_{E_b} \otimes \Gamma_{E_c^*})_a = \Gamma_{R_a}$, where a denotes the direction of light propagation. Among them, $(\Gamma_{E_x} \otimes \Gamma_{E_y^*})_z = \Gamma_{R_z} = B_2$, $(\Gamma_{E_y} \otimes \Gamma_{E_z^*})_x = \Gamma_{R_x} = B_1$, and $(\Gamma_{E_z} \otimes \Gamma_{E_x^*})_y = \Gamma_{R_y} = A_2$. The IC conductivity $\eta^{(2)}$ has two independent nonzero tensors, $\eta^x_{xy} \neq 0$ and $\eta^z_{yz} \neq 0$, as shown in Table S3. Moreover, the chirality of CPL can reverse the direction of the current, due to Berry curvature $\Omega^{bc}_{mn} = i(r^b_{mn}r^c_{nm} - r^c_{mn}r^b_{nm}) = -\Omega^{cb}_{mn}$, resulting in $\eta^x_{xy} = -\eta^x_{yx}$ and $\eta^z_{yz} = -\eta^z_{zy}$ in IC conductivity.

We computed the SC photoconductivity tensor under LPL and the IC photoconductivity tensor under CPL, as depicted in Figure S3. We can observe that the computational results are entirely consistent with the preceding group theory analysis. As shown in Figure 2a,b, the SC $\sigma^x_{xx} = 0$ and $\sigma^y_{xx} \neq 0$ ($\sigma^y_{yy} \neq 0$, $\sigma^y_{zz} \neq 0$), while the IC $\tau\eta^x_{xy} \neq 0$ and $\tau\eta^y_{xy} = 0$. When the incident photon energy $\hbar\omega$ = 0.47 eV, σ^y_{xx} = 52 μA/V^2; $\hbar\omega$ = 0.53 eV, $\tau\eta^x_{xy}$ = 5602 μA/V^2. Furthermore, we computed the photoconductivity σ^y_{xx} and $\tau\eta^x_{xy}$ of T-XY, as depicted in Figure S4. In T-XY, the σ^y_{xx} photoconductivity ranges from a minimum of 18 μA/V^2 (T-SnS) to a maximum of 135 μA/V^2 (T-BiSb), while $\tau\eta^x_{xy}$ ranges from a minimum of 811 μA/V^2 (T-SnS) to a maximum of 5602 μA/V^2 (T-SbP). Typically, conventional semiconductor materials such as h-BN and 2H TMDs,[31,39] as well as ferroelectric materials like group IV monochalcogenides α-MX,[30,33] have a photoconductivity range of 10−10^2 μA/V^2. Compared to these materials, the piezoelectric material T-XY exhibits photoconductivity 1−2 orders of magnitude higher. A high photoconductivity implies a large photocurrent, which is highly desirable for the design of functional devices. With its excellent piezoelectric properties and strong nonlinear optical response, T-XY holds significant potential for applications in photodetectors, nonlinear sensors, and flexible optoelectronics.

We can further uncover the microscopic mechanisms of photocurrent generation by analyzing the physical quantities within the conductivity. Here, we only consider the physical quantities between the highest valence band (v) and the lowest conduction band (c), which yields the same conclusions as considering all of the bands. The σ^x_{xx} and σ^y_{xx} photoconductivity in the SC and the $\boldsymbol{k}$-solved shift vector $R_{cv}(\boldsymbol{k})$ are shown in Figure 2b,c, respectively, with both exhibiting the same transition rate $r^x_{cv}r^x_{vc}(\boldsymbol{k})$, as depicted in Figure S5a. We clearly observe that the shift vectors in the x- and y-directions exhibit different mirror symmetries. The shift vectors $R^{x,x}_{cv}(\boldsymbol{k})$ and $R^{y,x}_{cv}(\boldsymbol{k})$ with respect to mirror M_{k_y} (perpendicular to k_y) are antisymmetric and symmetric, respectively, The transition rate $r^x_{cv}r^x_{vc}(\boldsymbol{k})$ exhibits M_{k_y} symmetry. Therefore, the integral term $R^{x,x}_{cv}(\boldsymbol{k})r^x_{cv}r^x_{vc}(\boldsymbol{k})$ has opposite signs at $-\boldsymbol{k}$ and $+\boldsymbol{k}$, and the conductivity integrates over the Brillouin zone to zero, yielding $\sigma^x_{xx} = 0$ (but $\sigma^y_{xx} \neq 0$). The $\tau\eta^x_{xy}$ and $\tau\eta^y_{xy}$ photoconductivity in the IC and the $\boldsymbol{k}$-solved velocity difference $\Delta_{vc}(\boldsymbol{k})$ are shown in Figure 2e,f, respectively. The Berry curvature $\Omega^{xy}_{cv}(\boldsymbol{k})$ is illustrated in Figure S5b. We observe that the velocity difference $\Delta^x_{vc}(\boldsymbol{k})$ is mirror symmetric under M_{k_y}, $\Delta^y_{vc}(\boldsymbol{k})$ is mirror antisymmetric, and $\Omega^{xy}_{cv}(\boldsymbol{k})$ is mirror symmetric. Hence, under the CPL-xy, $\tau\eta^x_{xy} \neq 0$ but $\tau\eta^y_{xy} = 0$.

Adding a detail of note, the group theory analysis indicated that η^z_{yz} is a nonzero photoconductivity. However, the computed conductivity for $\tau\eta^z_{yz}$ is found to be very small. To understand this finding, we computed the velocity difference $\Delta^z_{vc}(\boldsymbol{k})$ and the Berry curvature $\Omega^{yz}_{cv}(\boldsymbol{k})$ for $\tau\eta^z_{yz}$, as shown in Figure S5c,d. We note that $\tau\eta^y_{xy} = 0$ due to symmetry constraints, the $\tau\eta^z_{yz} \sim 0$ arises from integration terms in the conductivity being very small, with $\Delta^z_{vc}(\boldsymbol{k}) \sim 10^{-6}$ eV·Å, and $\Omega^{yz}_{cv}(\boldsymbol{k}) \sim 0.1$ Å^2. Therefore, conductivity tensors not constrained by symmetry can also yield extremely small values.

We investigate the spin degree of freedom of electrons, as well as the generation of spin currents in the context of the BSPV effect. Under the P-symmetry, $Ps^i_{mn}(\boldsymbol{k}) = s^i_{mn}(-\boldsymbol{k})$, $Pj^i_{mn}(\boldsymbol{k}) = -j^i_{mn}(-\boldsymbol{k})$, $P\Delta j^i_{mn}(\boldsymbol{k}) = -\Delta j^i_{mn}(-\boldsymbol{k})$, and $Pg_{mn}(\boldsymbol{k}) = g_{mn}(-\boldsymbol{k})$; $\Delta j^{a,i}_{mn}g^{bc}_{mn}$ in σ^{a,S^i}_{bc} and the numerator $j^{a,i}_{mn}v^b_{lm}v^c_{nl}$ in η^{a,S^i}_{bc} are both odd functions in momentum space. For materials with P-symmetry, both charge currents and spin currents will vanish. Under the T-symmetry, $Ts^i_{mn}(\boldsymbol{k}) = -s^{i^*}_{mn}(-\boldsymbol{k})$, $Tj^i_{mn}(\boldsymbol{k}) = j^{i^*}_{mn}(-\boldsymbol{k})$, $T\Delta j^i_{mn}(\boldsymbol{k}) = \Delta j^{i^*}_{mn}(-\boldsymbol{k})$, and $Tg_{mn}(\boldsymbol{k}) = g_{mn}(-\boldsymbol{k})$. The real parts of $\Delta j^{a,i}_{mn}g^{bc}_{mn}$ and $j^{a,i}_{mn}v^b_{lm}v^c_{nl}$ are even functions, while the imaginary parts are odd functions. Materials with T-symmetry may exhibit both charge currents and spin currents. It is noteworthy that due to the intrinsic property of spin, $s^i_{mn}(\boldsymbol{k}) = -s^{i^*}_{mn}(-\boldsymbol{k})$, charge currents and spin currents exhibit opposite trends. In systems with broken P-symmetry and preserved T-symmetry, spin currents generated by LPL illumination exhibit an injection-like behavior, while spin currents induced by CPL are shift-like.

In general, once the P-symmetry of the material is broken, both charge currents and spin currents are generated simultaneously. However, in practical research and applications, there is a strong desire to generate a pure spin current. In addition to preserving the T-symmetry, monolayer T-SbP also exhibits the M_x mirror symmetry (perpendicular to the x-axis). Under the mirror symmetry M_x,

$$M_x v^a_{mn}(k_x, k_y) = (-1)^{\delta(x-a)} v^a_{mn}(-k_x, k_y)$$

$$M_x s^i_{mn}(k_x, k_y) = -(-1)^{\delta(x-i)} s^i_{mn}(-k_x, k_y)$$

Here we only consider the spin component s^z for $i = z$. Under LPL illumination,

$$M_x R^{a,b}_{nm}r^b_{nm}r^c_{mn}(k_x, k_y) = (-1)^{\delta_{x,abc}} R^{a,b}_{nm}r^b_{nm}r^c_{mn}(-k_x, k_y)$$

$$M_x \Delta j^{a,z}_{mn}g^{bc}_{nm}(k_x, k_y) = -(-1)^{\delta_{x,z}}(-1)^{\delta_{x,abc}} \Delta j^{a,z}_{mn}g^{bc}_{nm}(-k_x, k_y)$$

For charge current, when there is an odd number of x in a, b, and c, the current vanishes, such as $\sigma^x_{xx} = 0$, but $\sigma^y_{xx} \neq 0$. For spin current, when there is an even number of x in a, b, and c, the current vanishes, such as $\sigma^{x,S^z}_{xx} \neq 0$, but $\sigma^{y,S^z}_{xx} = 0$. In addition, under CPL illumination, according to the symmetry analysis of the physical quantities mentioned above, for charge

https://doi.org/10.1021/acs.jpclett.4c01257
J. Phys. Chem. Lett. 2024, 15, 6099−6107

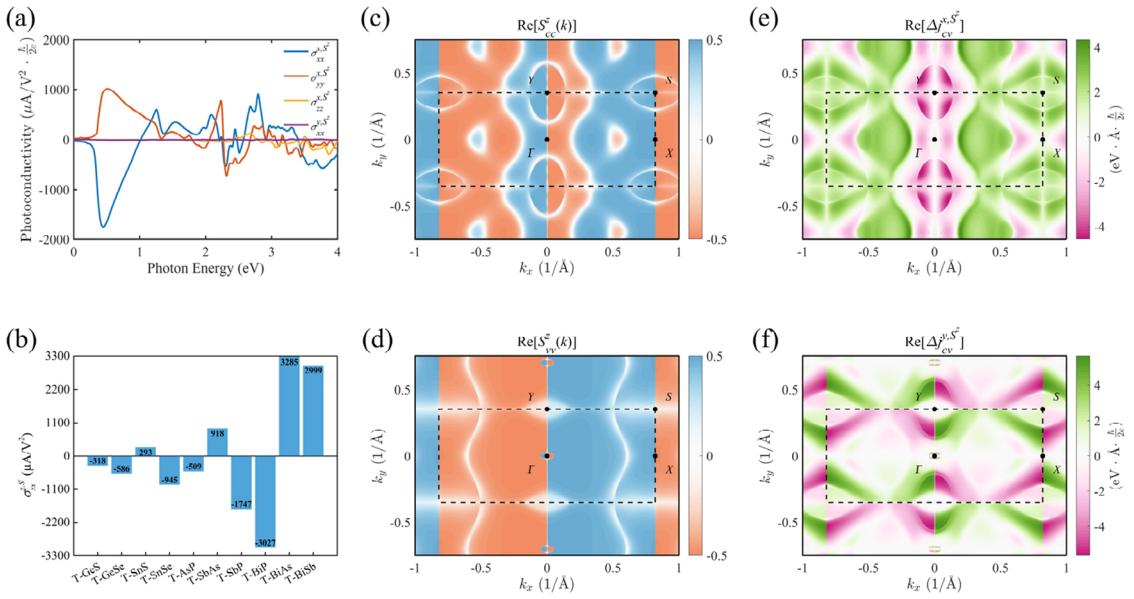

Figure 3. Spin current and the distribution of physical quantities in momentum space for T-SbP. (a) Under LPL, spin current photoconductivity σ_{xx}^{x,S^z}, σ_{yy}^{x,S^z}, σ_{zz}^{x,S^z}, and σ_{xx}^{y,S^z}. (b) Photoconductivity σ_{xx}^{x,S^z} for T-XY, with incident light energy ranging from 0 to 4 eV. (c, d) Representations of the spin texture on the lowest conduction band and the highest valence band, respectively. (e) $\boldsymbol{k}$-solved spin velocity difference of σ_{xx}^{x,S^z}. (f) $\boldsymbol{k}$-solved spin velocity difference of σ_{xx}^{y,S^z}.

current, $\tau\eta_{xy}^{x} \neq 0$ and $\tau\eta_{xy}^{y} = 0$, and for spin current, $\eta_{xy}^{x,S^z} = 0$ and $\eta_{xy}^{y,S^z} \neq 0$. Therefore, we can infer that the mirror symmetry of the structure can generate a pure spin current, such as $\sigma_{xx}^{x} = 0$ and $\sigma_{xx}^{x,S^z} \neq 0$. In LPL-$xx$, there is no charge current in the x-direction, so a pure spin current is generated. On the other hand, in addition to the special structural symmetry, the electron spin polarization is also crucial for the spin current. We have calculated the spin texture S_{nm}^{z} of T-SbP at the lowest conduction band and the highest valence band, where $S_{nm}^{z} = 1/2\langle n|\sigma^{z}|m\rangle$, as illustrated in Figure 3c,d. We can clearly observe that $S^z \cong \pm 1/2$ at all $\boldsymbol{k}$-points, and the polarization direction of the spin is opposite at $\boldsymbol{k}$- and $-\boldsymbol{k}$-points. This conclusion is consistent with the recent research reported by Guo et al., indicating that T-SbP exhibits intrinsic persistent spin helix,[24] where the spin only possesses the out-of-plane component S^z.

We calculated all spin photocurrent conductivity tensors of T-SbP under LPL and CPL illumination, as shown in Figure S6. The computational results align perfectly with the symmetry analysis mentioned above. As shown in Figure 3a, at photon energy $\hbar\omega$ = 0.45 eV, $\sigma_{xx}^{x,S^z} = -1747\ \mu A/V^2{\cdot}\hbar/2e$, while $\sigma_{xx}^{y,S^z} = 0$. For the charge current, we know that $\sigma_{xx}^{x} = 0$, while $\sigma_{xx}^{y} \neq 0$. We can draw an important inference that under linearly polarized light, the charge current in the mirror symmetric x-direction is zero. However, this does not imply that the electrons are fixed and immobile. In fact, electrons with spin up and spin down move in opposite directions along the x-axis, resulting in a total charge current cancellation, thus generating a pure spin current. Conversely, in the y-direction, electrons with spin up and spin down move in the same direction, resulting in the disappearance of spin polarization. The charge current is nonzero, while the spin current is zero. The spin current conductivity tensor σ_{xx}^{x,S^z} of T-XY is illustrated in Figure 3b (σ_{yy}^{x,S^z} shown in Figure S7a). Among them, the conductivity of T-BiAs is the highest, with $\sigma_{xx}^{x,S^z} = 3285\ \mu A/V^2{\cdot}\hbar/2e$. According to previous studies on spin current, the semiconductor 2H-MoS_2 ~ 120 $\mu A/V^2{\cdot}\hbar/2e$,[32] the antiferromagnetic (AFM) $MnPSe_3$ ~ 10 $\mu A/V^2{\cdot}\hbar/2e$,[40] and the magnetic topological quantum material bilayer AFM-$MnBi_2Te_4$ ~ 40 $\mu A/V^2{\cdot}\hbar/2e$.[41] The spin current of T-XY is tens of times larger than them. T-XY possesses a significant spin current, enabling it to have vast applications in spintronics, as well as in next generation low-energy devices and quantum computing.

The distribution of physical quantities in momentum space within the conductivity can provide further evidence for the earlier inference regarding the spin current. We calculated the spin velocity difference in σ_{xx}^{x,S^z} and σ_{xx}^{y,S^z}, depicted respectively in Figure 3e,f. They have the same quantum metric $g_{cv}^{xx} = \{r_{cv}^{x}, r_{vc}^{x}\}$, as shown in Figure S7b. We observe that the quantum metric satisfies $g_{cv}^{xx}(k_x, k_y) = g_{cv}^{xx}(-k_x, k_y)$. In the x-direction, the spin velocity difference is $\Delta j_{cv}^{x,S^z}(k_x, k_y) = \Delta j_{cv}^{x,S^z}(-k_x, k_y)$. In the y-direction, the spin velocity difference is such that $\Delta j_{cv}^{y,S^z}(k_x, k_y) = -\Delta j_{cv}^{y,S^z}(-k_x, k_y)$. Therefore, along the mirror M_x direction (y-direction), the spin current vanishes, while perpendicular to the mirror M_x direction (x-direction), the spin current is nonzero. Compared to traditional magnetic materials, utilizing piezoelectric materials to generate spin currents offers advantages such as stable optoelectronic properties (even under high-temperature and strong magnetic field conditions), high efficiency, and strong tunability.[42−44]

The development of effective strategies for controlling the charge current and spin current in second-order nonlinear optical responses is highly significant for the practical application and design of materials in device engineering.

https://doi.org/10.1021/acs.jpclett.4c01257
J. Phys. Chem. Lett. 2024, 15, 6099−6107

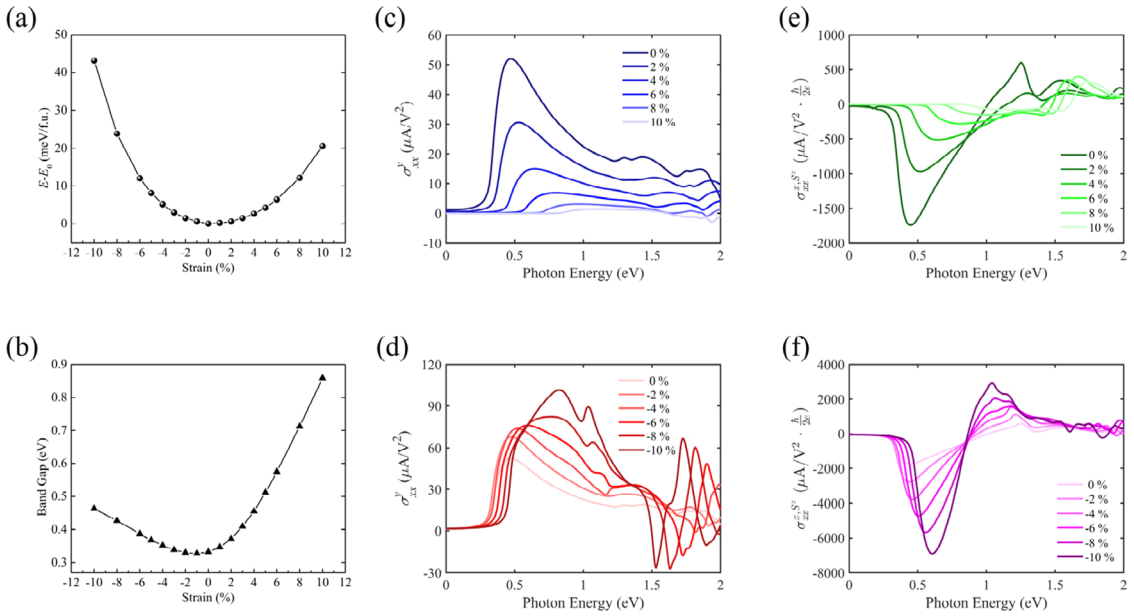

Figure 4. Charge current and spin current of T-SbP under uniaxial strain (along the *y*-direction). (a) Relationship between the change in total energy per unit cell ($\Delta E = E - E_0$) and strain, where E_0 is the total energy in the unstrained state. (b) Plot illustrating the relationship between the band gap and strain. (c, d) Evolution of the charge current conductivity σ_{xx}^{y} under tensile and compressive strains, respectively. (e, f) Evolution of the spin current conductivity σ_{xx}^{x,S^z} under tensile and compressive strains, respectively.

Typically, the optoelectronic properties of materials can be tuned by external stimuli, such as applying strain, external electric field, doping, and so forth.[45−47] The T-XY is an excellent piezoelectric material, attributed to its unique triple-staggered layer folded structure. Its in-plane piezoelectric coefficient (T-SnS, $d_{11} \sim 452$ pm/V) larger than that of most 2D piezoelectric materials,[23] such as 2*H*-MoS_2 (3.73 pm/V),[48] CdO (23.7 pm/V),[49] α-SnSe (250.5 pm/V),[50] etc. It is evident that strain engineering will be a reliable and efficient method for controlling the electronic and optical properties of T-XY. Over the past few years, the bulk piezophotovoltaic effect has been associated with piezoelectric materials when they are subjected to strain engineering techniques.[51−53]

In this study, we apply uniaxial strain along the *y*-direction, using the material T-SbP as an example for illustration. As shown in Figure 4a, the plot represents the relationship between the change in total energy per unit cell ($\Delta E = E - E_0$) and strain, where E is the total energy after applying strain and E_0 is the total energy without strain. Surprisingly, we can find that applying −10% compressive strain, the total energy of the per unit cell increases by only 43.2 meV, and at 10% tensile strain the total energy increases by only 20.6 meV. This further confirms that T-XY is an excellent piezoelectric material, with a highly flexible structure along the polarization direction. Additionally, this also indicates that T-XY maintains stable structure and performance under external strain stimuli. We also calculated the variation of the band gap under uniaxial strain, as shown in Figure 4b. Under compressive strain, the band gap initially slightly decreases and then monotonically increases with strain (<−3%). Under tensile strain, the band gap increases almost linearly with strain, reaching 0.86 eV at 10% strain.

Strain engineering can significantly alter the electronic properties of T-SbP. Following this, we will continue to explore the impact of strain on the BPV and BSPV effects in T-SbP. Under LPL illumination, the evolution of the charge current photoconductivity σ_{xx}^{y} with uniaxial tensile and compressive strains is shown in Figure 4c,d, respectively. When tensile strain is applied, there is a continuous reduction in the conductivity σ_{xx}^{y} as the strain increases. When 10% strain is reached, σ_{xx}^{y} decreases from 52 μA/V^2 (with $\hbar\omega$ = 0.47 eV) to 1.45 μA/V^2 (with $\hbar\omega$ = 1.12 eV), diminishing to nearly disappearance. Additionally, besides the decrease in the peak of conductivity, its position also undergoes a blue shift. For applied compressive strain, σ_{xx}^{y} increases continuously with increasing strain. Under −10% compressive strain, with $\hbar\omega$ = 0.83 eV, σ_{xx}^{y} = 101.8 μA/V^2, which is nearly double compared to that of the unstrained state. The evolution of the spin current conductivity σ_{xx}^{x,S^z} with strain is shown in Figure 4e,f. Similar to the charge current, the spin current decreases under tensile strain and increases under compressive strain. Especially, under compressive strain, σ_{xx}^{x,S^z} increases almost linearly with strain. Applying a small strain, such as −2%, yields σ_{xx}^{x,S^z} = −2776 μA/V^2·$\hbar/2e$ ($\hbar\omega$ = 0.44 eV), indicating a 59% increase in conductivity. When the compressive strain reaches −10%, σ_{xx}^{x,S^z} = −6914 μA/V^2·$\hbar/2e$ ($\hbar\omega$ = 0.61 eV), the conductivity increases by 296%. The charge current $\tau\eta_{xy}^{x}$ and spin current σ_{yy}^{x,S^z} exhibit similar trends under strain, as shown in Figure S8. Reviewing Figure 4a, it appears that T-XY can withstand stronger strains. We can make a reasonable inference that when tensile strain reaches a certain critical value (>10%), the photocurrent will vanish, thereby achieving the application of strain engineering in the on−off logic function of nonlinear photocurrents. Applying larger compressive strains (<−10%) may generate greater charge/spin currents to meet the requirements of device design.

The charge/spin currents exhibit systematic variations under strain engineering, and we attempt to uncover the underlying physical mechanisms. Initially, we calculated the differential

https://doi.org/10.1021/acs.jpclett.4c01257
J. Phys. Chem. Lett. 2024, 15, 6099−6107

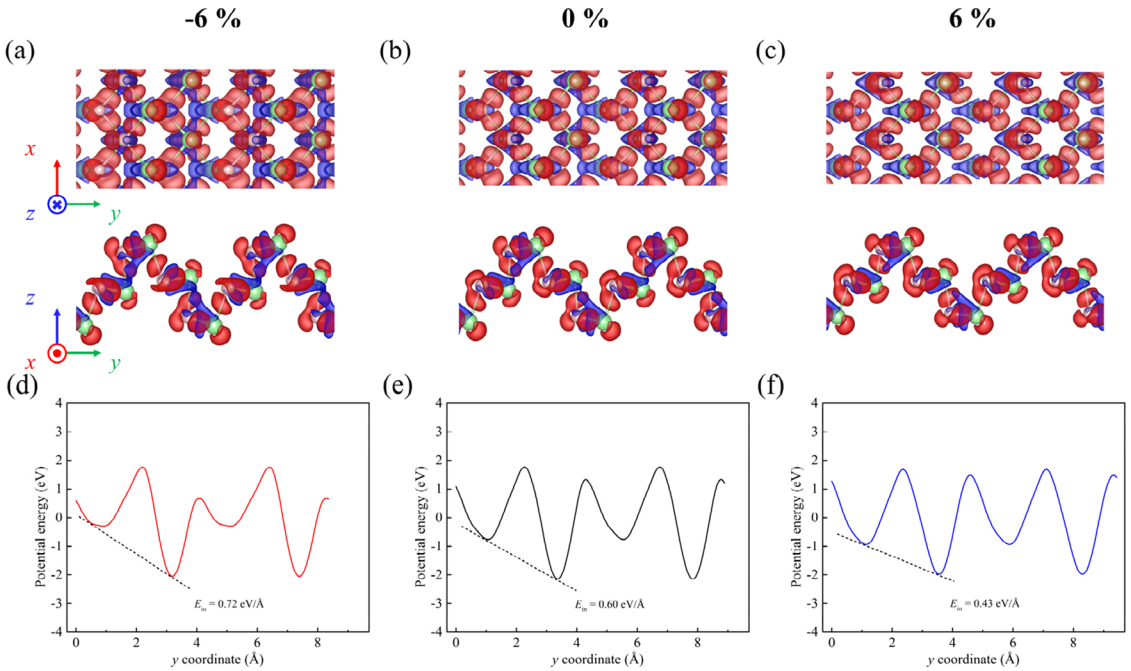

Figure 5. (a–c) Differential charge density plots of T-SbP at −6, 0, and 6% uniaxial strains, where red and blue represent electron accumulation and depletion, respectively. (d–f) Planar-averaged electrostatic potential energy along the *y*-direction of T-SbP under −6, 0, and 6% uniaxial strains, where E_{in} represents the built-in electric field along the *y*-direction.

charge density plots of T-SbP under −6, 0, and 6% uniaxial strains, as shown in Figure 5a–c, where the isosurfaces are shown in red for electron accumulation and in blue for electron depletion. It is noticeable that under compressive strain, the isosurfaces of accumulation (depletion) approach each other, which facilitates electron transport and leads to larger currents. Conversely, under tensile strain, the isosurfaces move away from each other, naturally resulting in a decrease in current. Alternatively, applying compressive strain causes the distances between Sb and P atoms in the structure to decrease, resulting in greater overlap of electron clouds, which facilitates the generation of larger currents. In contrast, under tensile strain, the distances between atoms increase, leading to smaller currents. Second, we calculated the planar-averaged electrostatic potential energy along the *y*-direction under −6, 0, and 6% uniaxial strains, as shown in Figure 5d–f. In the figure, E_{in} represents the built-in electric field along the *y*-direction, also known as the intrinsic polar field. The built-in electric field is defined as $E_{in} = \Delta\Phi/\Delta y$, where $\Delta\Phi$ represents the potential energy difference and Δy denotes the distance difference along the *y*-direction. In the absence of strain, the intrinsic structure yields E_{in} = 0.60 eV/Å. When applying −6% strain, E_{in} = 0.72 eV/Å, indicating an enhancement of the built-in electric field due to compressive strain. A stronger built-in electric field in the material can accelerate electron movement, leading to the generation of larger currents (as observed in the changes of σ_{xx}^{y} under compressive strain). For 6% tensile strain, E_{in} = 0.43 eV/Å, indicating a decrease in the built-in electric field. Consequently, the current will also decrease. Additionally, we also calculated the planar-averaged electrostatic potential energy along the *x*-direction after applying uniaxial strain along the *y*-direction, as shown in Figure S9. Under compressive strain, the potential energy along the *x*-direction decreases, while under tensile strain, it increases. When the potential energy decreases, the current will increase (as observed in the changes of σ_{xx}^{x,S^z} under compressive strain).

In summary, we have employed first-principles calculations and BPV/BSPV theories to investigate the second-order nonlinear optical response in the piezoelectric material T-XY. The SC photoconductivities of T-XY have five independent nonzero components under LPL illumination, while the IC photoconductivities have two independent nonzero components under CPL illumination. In the direction perpendicular to the mirror symmetry plane, electrons with opposite spins move in opposite directions, leading to the disappearance of charge current and the emergence of a pure spin current. The piezoelectric materials T-XY exhibit significant charge current and spin current in general. Among them, T-SbP exhibits the largest charge current $\tau\eta_{xy}^{x}$ = 5602 μA/V^2, while T-BiAs demonstrates the highest spin current σ_{xx}^{x,S^z} = 3285 μA/V^2·$\hbar$/2*e*, which are 1–2 orders greater than most other 2D materials. Furthermore, the photocurrent decreases under tensile strain, whereas it increases under compressive strain. The close proximity of atoms within the structure and the enhanced built-in electric field facilitate electron transport, resulting in a greater photocurrent. The piezoelectric material T-XY possesses excellent piezoelectric properties, as well as colossal and tunable nonlinear charge/spin photocurrents, thereby endowing it with broad potential applications in nonlinear optoelectronics and opto-spintronics.

■ ASSOCIATED CONTENT

Supporting Information

The Supporting Information is available free of charge at https://pubs.acs.org/doi/10.1021/acs.jpclett.4c01257.

Details of computational methods, lattice parameters, band structure, C_{2v} point group character table, direct product between irreducible representations, photo-

https://doi.org/10.1021/acs.jpclett.4c01257
J. Phys. Chem. Lett. 2024, 15, 6099−6107

conductivity of charge/spin currents, distribution plots of physical quantities in momentum space, and planar averaged electrostatic potential energy along the x-direction (PDF)

Transparent Peer Review report available (PDF)

AUTHOR INFORMATION

Corresponding Author

Yu-Jun Zhao − *Department of Physics and Key Laboratory of Advanced Energy Storage Materials of Guangdong Province, South China University of Technology, Guangzhou 510641, China;* orcid.org/0000-0002-6923-1099; Email: zhaoyj@scut.edu.cn

Authors

Chengwei Liao − *Department of Physics, South China University of Technology, Guangzhou 510641, China*

Minglong Wang − *Department of Physics, South China University of Technology, Guangzhou 510641, China*

Complete contact information is available at: https://pubs.acs.org/10.1021/acs.jpclett.4c01257

Notes

The authors declare no competing financial interest.

ACKNOWLEDGMENTS

This work is financially supported by National Natural Science Foundation of China (Grant No. 12074126). The computer times at the High Performance Computational center at South China University of Technology are gratefully acknowledged.

REFERENCES

(1) Glass, A. M.; von der Linde, D.; Negran, T. J. High-Voltage Bulk Photovoltaic Effect and the Photorefractive Process in $LiNbO_3$. *Appl. Phys. Lett.* **1974**, *25*, 233.

(2) Belinicher, V. I.; Sturman, B. I. The Photogalvanic Effect in Media Lacking a Center of Symmetry. *Sov. Phys. Usp.* **1980**, *23*, 199−223.

(3) Fridkin, V. M. Bulk Photovoltaic Effect in Noncentrosymmetric Crystals. *Crystallogr. Rep.* **2001**, *46*, 654−658.

(4) Grinberg, I.; West, D. V.; Torres, M.; Gou, G.; Stein, D. M.; Wu, L.; Chen, G.; Gallo, E. M.; Akbashev, A. R.; Davies, P. K.; Spanier, J. E.; Rappe, A. M. Perovskite Oxides for Visible-Light-Absorbing Ferroelectric and Photovoltaic Materials. *Nature* **2013**, *503*, 509−512.

(5) Liu, L.; Liu, W.; Cheng, B.; Cui, B.; Hu, J. Switchable Giant Bulk Photocurrents and Photo-Spin-Currents in Monolayer PT-Symmetric Antiferromagnet $MnPSe_3$. *J. Phys. Chem. Lett.* **2023**, *14*, 370−378.

(6) Yang, S. Y.; Seidel, J.; Byrnes, S. J.; Shafer, P.; Yang, C.-H.; Rossell, M. D.; Yu, P.; Chu, Y.-H.; Scott, J. F.; Ager, J. W.; Martin, L. W.; Ramesh, R. Above-Bandgap Voltages from Ferroelectric Photovoltaic Devices. *Nat. Nanotechnol.* **2010**, *5*, 143−147.

(7) Spanier, J. E.; Fridkin, V. M.; Rappe, A. M.; Akbashev, A. R.; Polemi, A.; Qi, Y.; Gu, Z.; Young, S. M.; Hawley, C. J.; Imbrenda, D.; Xiao, G.; Bennett-Jackson, A. L.; Johnson, C. L. Power Conversion Efficiency Exceeding the Shockley-Queisser Limit in a Ferroelectric Insulator. *Nat. Photonics* **2016**, *10*, 611.

(8) Zhang, Y. J.; Ideue, T.; Onga, M.; Qin, F.; Suzuki, R.; Zak, A.; Tenne, R.; Smet, J. H.; Iwasa, Y. Enhanced Intrinsic Photovoltaic Effect in Tungsten Disulfide Nanotubes. *Nature* **2019**, *570*, 349−353.

(9) Burger, A. M.; Agarwal, R.; Aprelev, A.; Schruba, E.; Gutierrez-Perez, A.; Fridkin, V. M.; Spanier, J. E. Direct Observation of Shift and Ballistic Photovoltaic Currents. *Sci. Adv.* **2019**, *5*, No. eaau5588.

(10) Daranciang, D.; et al. Ultrafast Photovoltaic Response in Ferroelectric Nanolayers. *Phys. Rev. Lett.* **2012**, *108*, 087601.

(11) Bhat, R. D. R.; Sipe, J. E. Optically Injected Spin Currents in Semiconductors. *Phys. Rev. Lett.* **2000**, *85*, 5432−5435.

(12) Young, S. M.; Zheng, F.; Rappe, A. M. Prediction of a Linear Spin Bulk Photovoltaic Effect in Antiferromagnets. *Phys. Rev. Lett.* **2013**, *110*, 057201.

(13) Yu, H.; Wu, Y.; Liu, G. B.; Xu, X.; Yao, W. Nonlinear Valley and Spin Currents from Fermi Pocket Anisotropy in 2D Crystals. *Phys. Rev. Lett.* **2014**, *113*, 156603.

(14) Hamamoto, K.; Ezawa, M.; Kim, K. W.; Morimoto, T.; Nagaosa, N. Nonlinear Spin Current Generation in Noncentrosymmetric Spin-Orbit Coupled Systems. *Phys. Rev. B* **2017**, *95*, 224430.

(15) Fei, R.; Yu, S.; Lu, Y.; Zhu, L.; Yang, L. Switchable Enhanced Spin Photocurrent in Rashba and Cubic Dresselhaus Ferroelectric Semiconductors. *Nano Lett.* **2021**, *21*, 2265−2271.

(16) Puebla, J.; Kim, J.; Kondou, K.; Otani, Y. Spintronic Devices for Energy Efficient Data Storage and Energy Harvesting. *Commun. Mater.* **2020**, *1*, 24.

(17) Ladd, T. D.; Jelezko, F.; Laflamme, R.; Nakamura, Y.; Monroe, C.; O'Brien, J. L. Quantum Computers. *Nature* **2010**, *464*, 45−53.

(18) Jungwirth, T.; Sinova, J.; Manchon, A.; Marti, X.; Wunderlich, J.; Felser, C. The Multiple Directions of Antiferromagnetic Spintronics. *Nat. Phys.* **2018**, *14*, 200−203.

(19) Young, S. M.; Rappe, A. M. First Principles Calculation of the Shift Current Photovoltaic Effect in Ferroelectrics. *Phys. Rev. Lett.* **2012**, *109*, 116601.

(20) Rangel, T.; Fregoso, B. M.; Mendoza, B. S.; Morimoto, T.; Moore, J. E.; Neaton, J. B. Large Bulk Photovoltaic Effect and Spontaneous Polarization of Single-Layer Monochalcogenides. *Phys. Rev. Lett.* **2017**, *119*, 067402.

(21) Wang, H.; Qian, X. Giant Optical Second Harmonic Generation in Two-Dimensional Multiferroics. *Nano Lett.* **2017**, *17*, 5027−5034.

(22) Qian, Z.; Zhou, J.; Wang, H.; Liu, S. Shift Current Response in Elemental Two-Dimensional Ferroelectrics. *npj Comput. Mater.* **2023**, *9*, 67.

(23) Lei, H.; Ouyang, T.; He, C. Y.; Li, J.; Tang, C. Monolayer Group IV Monochalcogenides T-MX (M = Sn, Ge; X = S, Se) with Fine Piezoelectric Performance and Stability. *Appl. Phys. Lett.* **2023**, *122*, 062903.

(24) Guo, S. D.; Feng, X. K.; Huang, D.; Chen, S.; Wang, G.; Ang, Y. S. Intrinsic Persistent Spin Texture in Two-Dimensional T-XY (X, Y = P, As, Sb, Bi; X ≠ Y). *Phys. Rev. B* **2023**, *108*, 075421.

(25) Bernevig, B. A.; Orenstein, J.; Zhang, S. C. Exact SU(2) Symmetry and Persistent Spin Helix in a Spin-Orbit Coupled System. *Phys. Rev. Lett.* **2006**, *97*, 236601.

(26) Kraut, W.; Von Baltz, R. Anomalous Bulk Photovoltaic Effect in Ferroelectrics: A Quadratic Response Theory. *Phys. Rev. B* **1979**, *19*, 1548−1554.

(27) Von Baltz, R.; Kraut, W. Theory of the Bulk Photovoltaic Effect in Pure Crystals. *Phys. Rev. B* **1981**, *23*, 5590−5596.

(28) Sipe, J. E.; Shkrebtii, A. I. Second-Order Optical Response in Semiconductors. *Phys. Rev. B* **2000**, *61*, 5337−5352.

(29) Ibañez-Azpiroz, J.; Tsirkin, S. S.; Souza, I. Ab Initio Aalculation of the Shift Photocurrent by Wannier Interpolation. *Phys. Rev. B* **2018**, *97*, 245143.

(30) Wang, H.; Qian, X. Ferroicity-Driven Nonlinear Photocurrent Switching in Time-Reversal Invariant Ferroic Materials. *Sci. Adv.* **2019**, *5*, No. eaav9743.

(31) Xu, H.; Wang, H.; Zhou, J.; Guo, Y.; Kong, J.; Li, J. Colossal Switchable Photocurrents in Topological Janus Transition Metal Dichalcogenides. *npj Comput. Mater.* **2021**, *7*, 31.

(32) Xu, H.; Wang, H.; Zhou, J.; Li, J. Pure Spin Photocurrent in Non-Centrosymmetric Crystals: Bulk Spin Photovoltaic Effect. *Nat. Commun.* **2021**, *12*, 4330.

(33) Mu, X.; Pan, Y.; Zhou, J. Pure Bulk Orbital and Spin Photocurrent in Two-Dimensional Ferroelectric Materials. *npj Comput. Mater.* **2021**, *7*, 61.

(34) Shi, Y.; Zhou, J. Coherence Control of Directional Nonlinear Photocurrent in Spatially Symmetric Systems. *Phys. Rev. B* **2021**, *104*, 155146.
(35) Bernevig, B. A.; Zhang, S. C. Quantum Spin Hall Effect. *Phys. Rev. Lett.* **2006**, *96*, 106802.
(36) Zhao, T.; Guo, J.; Li, T.; Wang, Z.; Peng, M.; Zhong, F.; Chen, Y.; Yu, Y.; Xu, T.; Xie, R.; Gao, P.; Wang, X.; Hu, W. Substrate Engineering for Wafer-Scale Two-Dimensional Material Growth: Strategies, Mechanisms, and Perspectives. *Chem. Soc. Rev.* **2023**, *52*, 1650−1671.
(37) Zhang, J.; Wang, F.; Shenoy, V. B.; Tang, M.; Lou, J. Towards Controlled Synthesis of 2D Crystals by Chemical Vapor Deposition (CVD). *Mater. Today* **2020**, *40*, 132−139.
(38) Dresselhaus, M. S.; Dresselhaus, G.; Jorio, A. *Group Theory: Application to the Physics of Condensed Matter*. Springer: Berlin and Heidelberg, Germany, 2007. DOI: 10.1007/978-3-540-32899-5.
(39) Wang, C.; Liu, X.; Kang, L.; Gu, B. L.; Xu, Y.; Duan, W. First-Principles Calculation of Nonlinear Optical Responses by Wannier Interpolation. *Phys. Rev. B* **2017**, *96*, 115147.
(40) Xue, Q.; Mu, X.; Sun, Y.; Zhou, J. Valley Contrasting Bulk Photovoltaic Effect in a PT-Symmetric $MnPSe_3$ Monolayer. *Phys. Rev. B* **2023**, *107*, 245404.
(41) Mu, X.; Xue, Q.; Sun, Y.; Zhou, J. Magnetic Proximity Enabled Bulk Photovoltaic Effects in van der Waals Heterostructures. *Phys. Rev. Research* **2023**, *5*, 013001.
(42) Meng, Y.; Chen, G.; Huang, M. Piezoelectric Materials: Properties, Advancements, and Design Strategies for High-Temperature Applications. *Nanomaterials* **2022**, *12*, 1171.
(43) Li, T.; Lee, P. S. Piezoelectric Energy Harvesting Technology: From Materials, Structures, to Applications. *Small Struct* **2022**, *3*, 2100128.
(44) Yao, Z.; Deng, J.; Li, L. Piezoelectric Performance Regulation from 2D Materials to Devices. *Matter* **2024**, *7*, 855−888.
(45) Jiang, J.; Chen, Z.; Hu, Y.; Xiang, Y.; Zhang, L.; Wang, Y.; Wang, G. C.; Shi, J. Flexo-Photovoltaic Effect in MoS_2. *Nat. Nanotechnol.* **2021**, *16*, 894.
(46) Wang, H.; Qian, X. Electrically and Magnetically Switchable Nonlinear Photocurrent in *PT*-Symmetric Magnetic Topological Quantum Materials. *npj Comput. Mater.* **2020**, *6*, 199.
(47) Strasser, A.; Wang, H.; Qian, X. Nonlinear Optical and Photocurrent Responses in Janus MoSSe Monolayer and MoS_2-MoSSe van der Waals Heterostructure. *Nano Lett.* **2022**, *22*, 4145−4152.
(48) Duerloo, K. A. N.; Ong, M. T.; Reed, E. J. Intrinsic Piezoelectricity in Two-Dimensional Materials. *J. Phys. Chem. Lett.* **2012**, *3*, 2871−2876.
(49) Alyoruk, M. M. Piezoelectric Properties of Monolayer II-VI Group Oxides by First-Principles Calculations. *Phys. Status Solidi B* **2016**, *253*, 2534−2539.
(50) Fei, R.; Li, W.; Li, J.; Yang, L. Giant Piezoelectricity of Monolayer Group IV Monochalcogenides: SnSe, SnS, GeSe, and GeS. *Appl. Phys. Lett.* **2015**, *107*, 173104.
(51) Nadupalli, S.; Kreisel, J.; Granzow, T. Increasing Bulk Photovoltaic Current by Strain Tuning. *Sci. Adv.* **2019**, *5*, No. eaau9199.
(52) Schankler, A. M.; Gao, L.; Rappe, A. M. Large Bulk Piezophotovoltaic Effect of Monolayer 2*H*-MoS_2. *J. Phys. Chem. Lett.* **2021**, *12*, 1244−1249.
(53) Dong, Y.; Yang, M. M.; Yoshii, M.; Matsuoka, S.; Kitamura, S.; Hasegawa, T.; Ogawa, N.; Morimoto, T.; Ideue, T.; Iwasa, Y. Giant Bulk Piezophotovoltaic Effect in 3*R*-MoS_2. *Nat. Nanotechnol.* **2023**, *18*, 36−41.

https://doi.org/10.1021/acs.jpclett.4c01257
J. Phys. Chem. Lett. 2024, 15, 6099−6107